A&A 521, A79 (2010)
DOI: 10.1051/0004-6361/201014836

Astronomy & Astrophysics

High-resolution X-ray spectroscopy of the interstellar medium

XMM-Newton observation of the LMXB GS 1826−238

C. Pinto[1], J. S. Kaastra[1,2], E. Costantini[1], and F. Verbunt[2]

[1] SRON Netherlands Institute for Space Research, Sorbonnelaan 2, 3584 CA Utrecht, The Netherlands
e-mail: c.pinto@sron.nl
[2] Astronomical Institute, Utrecht University, PO Box 80000, 3508 TA Utrecht, The Netherlands

Received 21 April 2010 / Accepted 13 July 2010

ABSTRACT

Aims. The interstellar medium (ISM) has a multiphase structure characterized by gas, dust, and molecules. The gas can be found in different charge states: neutral, weakly ionized (warm) and highly ionized (hot). It is possible to probe the multiphase ISM through the observation of its absorption lines and edges in the X-ray spectra of background sources.
Methods. We present a high-quality RGS spectrum of the low-mass X-ray binary GS 1826−238 with an unprecedentedly detailed treatment of the absorption features caused by the dust and both the neutral and ionized gas of the ISM. We constrain the column density ratios within the different phases of the ISM and measure the abundances of elements such as O, Ne, Fe, and Mg.
Results. We found significant deviations from the protosolar abundances: oxygen is over-abundant by a factor 1.23 ± 0.05, neon by 1.75 ± 0.11, iron by 1.37 ± 0.17, and magnesium by 2.45 ± 0.35. The abundances are consistent with the measured metallicity gradient in our Galaxy: the ISM appears to be metal-rich in the inner regions. The spectrum also shows the presence of warm and hot ionized gas. The gas column has a total ionization degree of less than 10%. We also show that dust plays an important role as expected from the position of GS 1826−238: most iron appears to be bound in dust grains, while 10−40% of oxygen consist of a mixture of dust and molecules.

Key words. ISM: abundances – dust, extinction – ISM: structure – local interstellar matter – X-rays: ISM – techniques: spectroscopic

1. Introduction

The interstellar medium of our Galaxy (ISM) is a mixture of dust and gas in the form of atoms, molecules, ions, and electrons. It manifests itself primarily through obscuration, reddening and polarization of starlight and the formation of absorption lines in stellar spectra, and secondly through various emission mechanisms (broadband continuum and line emission). The gas is found in both neutral and ionized phases (for a review, see Ferrière 2001). The neutral phase is a blend of *cold molecular gas* ($T \sim 20$−50 K), found in the so-called dark clouds, and *cold atomic gas* ($T \sim 100$ K) inherent in the diffuse clouds, while the *warm atomic gas* has temperatures of up to 10^4 K. The atomic gas is well traced by H I and mainly concentrated in the Galactic plane with clouds up to few hundreds pc above it. The *warm ionized gas* is a weakly ionized gas, with a temperature of $\sim 10^4$ K. It is mainly traced by Hα-line emission and pulsar dispersion measures; it can reach a vertical height of 1 kpc. The *hot ionized gas* is characterized by temperatures of about 10^6 K. It is heated by supernovae and stellar winds from massive stars; it gives rise to high-ionization absorption lines and the soft X-ray background emission. The study of the ISM is very interesting because of its connection with the evolution of the entire Galaxy: the stellar evolution enriches the interstellar medium with heavy elements, while the ISM acts as a source of matter for the star-forming regions.

High-resolution X-ray spectroscopy has become a powerful diagnostic tool for constraining the chemical and physical properties of the ISM. Through the study of the X-ray absorption lines in the spectra of background sources it is possible to probe the various phases of the ISM of the Galaxy. First of all, the K-shell transitions of low-Z elements, such as oxygen and neon, and the L-shell transitions of iron fall inside the soft X-ray energy band. Secondly, the different charge states for each element allow us to constrain the multiphase ISM, e.g. its ionization state and temperature distribution.

Schattenburg & Canizares (1986) first measured ISM absorption edges in the X-ray band with the *Einstein Observatory* and found features consistent with the O I 1s–2p line and traces of O II. After the launch of the *XMM-Newton* and *Chandra* satellites a new era for the ISM study opened up. The grating spectrometers onboard these satellites, RGS and LETGS/HETGS respectively, provide a spectral resolution that is high enough to resolve the main absorption edges and lines. Recently, Yao et al. (2009) found high-ionization absorption lines of ions such as O VI to O VIII and Ne VIII to Ne X in the HETGS spectrum of the low-mass X-ray binary Cyg X-2, and argued that the bulk of the O VI should originate from the conductive interface between the cool and the hot gas. Other work has revealed a complex structure around the oxygen K-shell absorption edge (Paerels et al. 2001; de Vries et al. 2003; Juett et al. 2004). Costantini et al. (2005) argued that the feature of the scattering halo of Cyg X-2 near the O I K-edge can be attributed to dust towards the source, with a major contribution from silicates such as olivine and pyroxene. In their paper on Sco X-1, observed with *XMM-Newton*, de Vries & Costantini (2009) found clear indications of extended X-ray absorption fine structures (EXAFS) near the absorption edge of oxygen.

Table 1. Observations used in this paper.

ID	Date	Length (ks)	RGS (ks)	PN (ks)
0150390101	2003 April 6	108	67.8	63.8
0150390301	2003 April 8	92	77.8	67.8

Notes. We report the total exposure length together with the net exposure time remaining after screening of the background and removal of bursts.

In this work we report the detection of absorption lines and edges in the high-quality spectrum of the low-mass X-ray binary (LMXB) GS 1826−238 obtained with the *XMM-Newton* Reflection Grating Spectrometer (RGS, den Herder et al. 2001). In order to constrain the continuum parameters we also used the EPIC-pn (Strüder et al. 2001) dataset of this source. Thompson et al. (2008), using the *XMM-Newton* and RXTE observations of April 2003, derived a high unabsorbed bolometric flux $F \sim 3.5 \times 10^{-12}$ W m^{-2}. The source is well suited for the analysis of the ISM also because of its column density $N_{\rm H} \sim 4 \times 10^{25}$ m^{-2} (see Table 3), which is sufficiently high to produce prominent O and Fe edges. We assume the distance of the source to be 6.1 ± 0.2 kpc (Heger et al. 2007).

We analyze the absorption in the spectrum as follows. We first remove the bursts, because they add a strongly variable component to the spectrum. Then we determine the source continuum by simultaneously fitting EPIC and RGS data. In a second instance we use only the high-resolution RGS spectra to constrain the absorption contributions. We search for statistically significant features by adding several absorbers in sequence: cold gas, warm gas, hot gas, dust, and molecules. All of these appear to be important.

2. Observations and data reduction

The source GS 1826−238 (Galactic coordinates $l = 9\overset{\circ}{.}27$, $b = -6\overset{\circ}{.}09$) has been observed twice with *XMM-Newton* for a total length of 200 ks (see Table 1 for details). The data are reduced with the *XMM-Newton* Science Analysis System (SAS) version 9.0.1.

GS 1826–238 is a bursting LMXB with a regular time separation between the bursts. Because the primary aim of the *XMM-Newton* observations was the study of the bursts, the EPIC-pn detector was operated in timing mode, which means that imaging is made only in one dimension, along the RAWX axis. Along the row direction (RAWY axis), data from a predefined area on one CCD chip are collapsed into a one-dimensional row for a fast read-out. Then source photons are extracted between RAWX values 30–45 and background photons are extracted between rows 2–16, as recommended by the standard procedure.

We produced pn lightcurves mainly to remove the burst intervals and to extract the spectra of the persistent part of the lightcurve. In the first observation nine bursts we detected, in the second observation seven bursts. We plot the burst profiles of these 16 bursts in Fig. 2. We estimate a mean duration of about 300 s for the bursts, and we removed for each burst 50 s before the peak to 250 s after it. Recently in't Zand et al. (2009) suggested a mean duration of about 1 ks for the bursts, but they also argued that after the first 100 s the inferred emission decreases sharply by at least one order of magnitude, contributing only about 3% to the fluence in the burst. After 250 s the flux of the burst has decreased by almost two orders of magnitude and its profile merges with the persistent lightcurve. Thus, by removing 300 s for each burst, we retain less than ∼1% burst emission, which is negligible compared to the persistent emission.

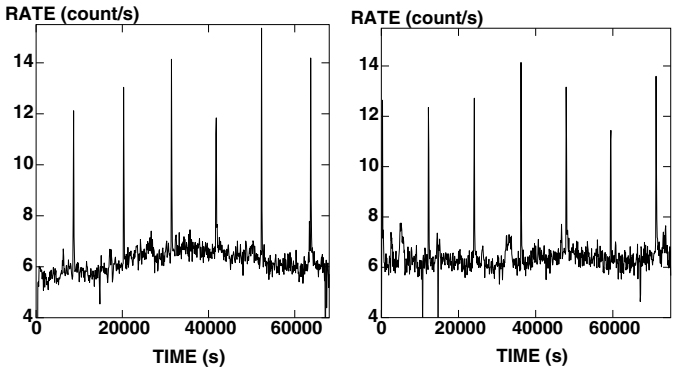

Fig. 1. Lightcurves of the first (*left*) and the second (*right*) observation with RGS1. Intervals with high background have already been taken out.The bursts are still shown for displaying purpose, but their contribution to the spectra are removed as described in the text. The plot shows the quasi-periodicity of the bursts and illustrates why GS 1826−238 is called the "clock-burster" LMXB (Ubertini et al. 1999).

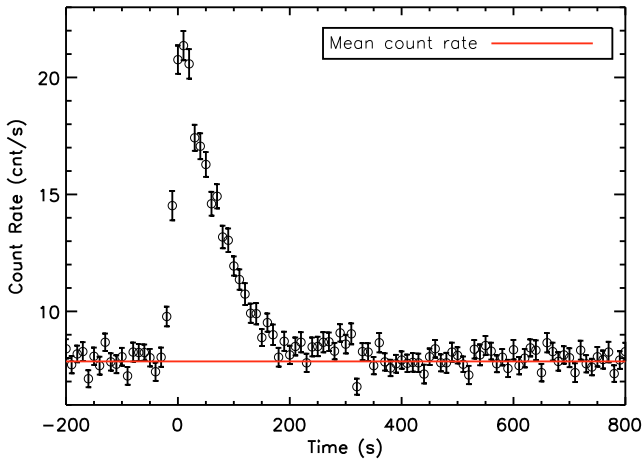

Fig. 2. Mean profile of the bursts in the RGS lightcurve of the first observation. The zero point of the timescale is centered on the burst profile peak. The red line represents the mean count rate of the 2 ks around the peaks.

We processed the RGS data with the SAS task *rgsproc*. We produced the lightcurves for the background in CCD9 following the XMM-SAS guide[1] in order to remove soft proton flares and spurious events. We created good time intervals (GTI) by removing intervals with count rates higher than 0.5 c s^{-1}. We reprocessed the data again with *rgsproc* by filtering them with the GTI for background screening and bursts removal. We extracted response matrices and spectra for the two observations. The final net exposure times are reported in Table 1.

Our analysis focuses on the 7–31 Å (0.4–1.77 keV) first order spectra of the RGS detector. In order to fit the spectral continuum properly, we also use the 0.5–10 keV EPIC spectra of both observations. We performed the spectral analysis with SPEX[2] version 2.01.05 (Kaastra et al. 1996). We scaled the elemental abundances to the protosolar abundances of Lodders (2003): N/H = 7.943×10^{-5}, O/H = 5.754×10^{-4}, Ne/H = 8.912×10^{-5},

[1] http://heasarc.nasa.gov/docs/xmm/abc/
[2] www.sron.nl/spex

Mg/H = 4.169×10^{-5}, Fe/H = 3.467×10^{-5}. We use the C-statistic throughout the paper and adopt 1σ errors.

3. Spectral modeling

The first step of the spectral analysis consists of the determination of the continuum emission and the dominant absorption component. The best way to do this is to fit the spectra of RGS and EPIC-pn simultaneously. The *XMM-Newton* cross-calibration is very complex, not only because of the different energy bands, but mainly because of their different features: RGS is sensitive in the soft X-ray energies with high spectral resolution, showing narrow absorption features, while pn has a low spectral resolution, therefore blurring the absorption features seen with RGS. EPIC-pn has a higher count rate compared to RGS and a broader energy band. The original RGS spectra are binned by a factor of 10 in this simultaneous fit. This is necessary to temporarily remove the narrow features due to the absorption lines. The pn spectra are resampled in bins of about 1/3 of the spectral resolution (*FWHM* ~ 50−150 eV between 0.5−10 keV), which is the optimal binning for most spectra.

A better local fit for absorption edges and lines is obtained from a separate RGS fit. In the RGS local fit we rebin the spectra only by a factor of two, i.e. about 1/3 *FWHM* (the first order RGS spectra provide a resolution of 0.06−0.07 Å). This gives at least 10 counts/bin and a bin size of about 0.02 Å.

3.1. Simultaneous EPIC–RGS fits

At first we followed the spectral modeling of Thompson et al. (2008). The continuum spectrum is modeled by emission from a blackbody and two comptonization models. The blackbody component arises from the thermal emission of the accretion disk around the neutron star. The first comptonization component (hereafter C1) describes the energy gain of the disk soft photons by scattering in the accretion disk corona. The second comptonization component C2 corresponds to scattered seed photons originating from regions closer to the NS surface, i.e. the boundary layer. Thompson et al. (2008) applied a neutral absorber to the continuum mentioned above and fitted *XMM-Newton*, Chandra, and RXTE data. For this purpose we used the *absm* model in SPEX: the model calculates the continuum transmission of neutral gas with cosmic abundances as published by Morrison & McCammon (1983). In our case the same model does not give a satisfactory fit, especially around the neon and oxygen edges, and cannot fit the O I line. This could be expected because the Morrison & McCammon (1983) model does not take into account the absorption lines and the possible variations in the abundances. Therefore we replace the *absm* component with a *hot* component, which describes the transmission through a layer of collisionally ionized plasma. At low temperatures it calculates the absorption of (almost) neutral gas (for further information see the SPEX manual). We left the temperature and the O, Ne, Mg, and Fe abundances of this absorber free in the fit. In the fits we ignored two small regions (17.2–17.7 Å and 22.7–23.2 Å), close to the iron and oxygen edges respectively. The presence of dust and molecules affects the fine structure of the edge, thus these regions will be analyzed with more complex models in Sect. 3.2.3. However, the ISM abundances were determined by the depth of the absorption edges, thus ignoring these small regions we could still constrain the abundances of these elements (Kaastra et al. 2009). Indeed, in Sect. 3.4 and Table 6 we will validate this assumption. We obtained a good fit with C-stat/d.o.f.[3] = 2451/1705 and 2579/1710 in the two observations (see Fig. 3). The parameters for both observations are listed in Table 2. We call this simple model, where the ISM is modeled with one (neutral) gas component, Model A. The abundances mostly agree between the two observations, but they are not reliable. In Sects. 3.2 and 3.4 we show that the RGS fit provides a column density higher by 10%, which significantly changes the abundance estimates. There are also small differences in the continuum parameters, such as the electron temperatures. Indeed we find different temperatures for both comptonization components (see Table 2). These small deviations affect the broadband spectral slope and forbid to fit the two EPIC-pn observations simultaneously, while this is possible with the RGS spectra.

Table 2. EPIC–RGS spectral fits to the persistent emission.

Par/component	OBS 1	OBS 2	Average value
absorber			
N_H (10^{25} m^{-2})	3.65 ± 0.05	3.68 ± 0.04	3.67 ± 0.03
kT (10^{-4} keV)	7.07 ± 0.10	7.22 ± 0.09	7.15 ± 0.07
O	1.471 ± 0.008	1.403 ± 0.008	1.437 ± 0.006
Ne	2.72 ± 0.04	2.64 ± 0.04	2.68 ± 0.03
Mg	0.81 ± 0.09	0.80 ± 0.09	0.80 ± 0.06
Fe	1.90 ± 0.03	2.01 ± 0.02	1.98 ± 0.02
blackbody			
flux (10^{-13} W m^{-2})	0.65 ± 0.10	0.55 ± 0.03	0.56 ± 0.03
kT_{bb} (keV)	0.170 ± 0.002	0.167 ± 0.002	0.168 ± 0.001
C1 comptonization			
flux (10^{-13} W m^{-2})	7.8 ± 0.3	7.7 ± 0.3	7.75 ± 0.21
kT_s (keV)	0.25 ± 0.02	0.24 ± 0.01	0.24 ± 0.01
kT_e (keV)	2.07 ± 0.05	2.38 ± 0.06	2.20 ± 0.04
τ	11.0 ± 0.6	9.3 ± 0.4	9.8 ± 0.3
C2 comptonization			
flux (10^{-13} W m^{-2})	0.9 ± 0.1	0.6 ± 0.1	0.75 ± 0.07
kT_s (keV)	0.50 ± 0.01	0.54 ± 0.01	0.52 ± 0.01
kT_e (keV)	9.4 ± 0.8	4.6 ± 0.5	5.9 ± 0.4
τ	≤0.5	≤0.7	–
C_{stat} / d.o.f.	2451/1705	2579/1710	–

Notes. Abundances are relative to the protosolar values of Lodders (2003). Fluxes are derived in the 0.3–10 keV band. We also report the weighted averages between the two observations. See also Fig. 3.

We also tested alternative continuum models in order to show that the adopted model is the best one. Thompson et al. (2008) showed that the spectral modeling of GS 1826−238 can be done with other continuum models: 1) blackbody emission plus a single comptonization component; 2) blackbody emission plus a cut-off powerlaw; 3) double comptonization plus a disk blackbody; 4) two comptonization components. We tested them on both spectra, but report here only the results for the first spectrum. The results for the other observation are similar. The models (1) and (2) give similar results, but with C-stat/d.o.f. = 3000/1709 the fit is worse than for our adopted Model A. Model (3) gives even worse fits. The final alternative model (4) gives an intermediate result C-stat/d.o.f. = 2625/1707.

3.2. The high-resolution RGS spectra

In Fig. 4 we plot the RGS spectrum of the persistent emission in the first and second observation. Several interesting features can be recognized. At 23.1 Å we see the absorption edge of the interstellar neutral oxygen, while the O I line is clearly visible at 23.5 Å. There is also a broad absorption feature close

[3] Here and hereafter d.o.f. means degrees of freedom.

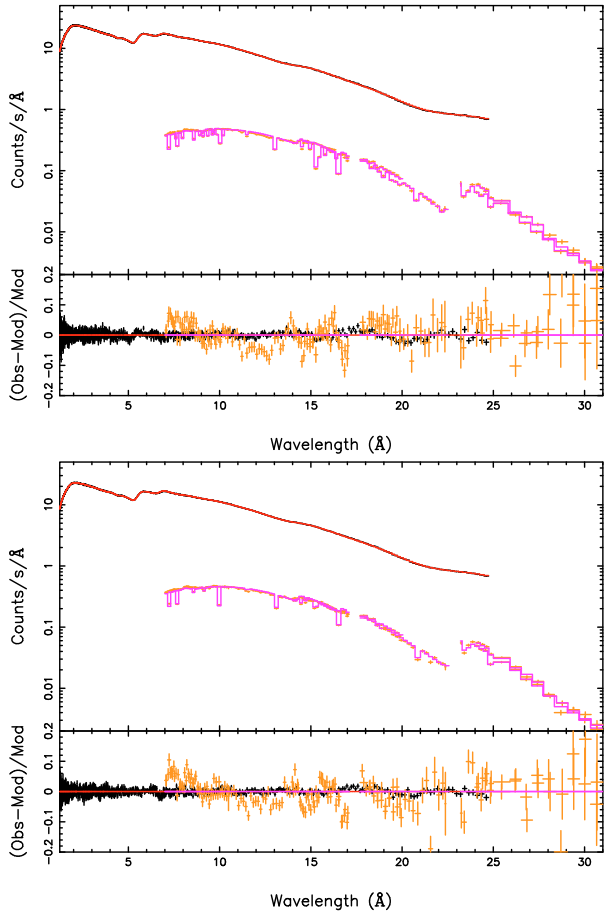

Fig. 3. Simultaneous RGS−EPIC best fits of the first (*top*) and the second (*bottom*) observations. The model used is Model A (see Sect. 3.1 and Table 2). *The upper panels* show from top to bottom the EPIC and RGS spectrum, respectively. *The lower panels* show the fit residuals (dark points with small error bars: EPIC). The dips in the count spectrum of the RGS correspond to bad columns in the RGS with lower sensitivity.

to the oxygen edge, which is clearly seen in the fits residuals, see Sect. 3.2.3 for a dedicated discussion. The K-edge of neon and L-edge of iron are easily recognized at 14.3 Å and 17.5 Å, respectively. We fitted the RGS spectra of the two observations simultaneously with Model A, freezing the shape of the continuum emission and leaving as free parameters the normalizations of the emission components and the parameters of the absorber. In the fits we still ignored the two small regions (17.2–17.7 Å and 22.7–23.2 Å), close to the iron and oxygen edges respectively (see Sect. 3.2.3 for the dedicated analysis). The results of the RGS spectral fits are shown in Table 3 and are referred to Model A. We also report the results of the fits obtained for each observation: the agreement between the parameters validates the simultaneous spectral fit. As expected, the residuals (Fig. 4) show large deviations in the spectral regions that we have temporarily removed: $\sim 4\sigma$ and $\sim 3\sigma$ near 17.4 Å and 23 Å, respectively. These features cannot be modeled with a pure-gas model and require the introduction of dust and molecular components in our model (see Sect. 3.2.3).

3.2.1. The neutral gas

The fits obtained with a simple model (a single gas component for the ISM) show that the ISM can be initially modeled with cold gas (see Table 2 and 3, Model A). It has a mean temperature of $kT \sim 6 \times 10^{-4}$ keV, i.e. about 7000 K, and provides the bulk of the warm atomic gas anticipated in the introduction. It is almost neutral, except for iron and magnesium: Mg II contributes 30% to the total magnesium column density, while Fe II accounts for 20% of the iron. A precise measure of the ratios Mg I/Mg II and Fe I/Fe II for our spectra is not possible. Near the magnesium edge the spectrum is noisy and the Mg I and Mg II edges are close, at 9.48 Å and 9.30 Å respectively, while near the iron edge the lines are unresolved and there is also a contribution from dust that affects the edge structure (see Sect. 3.2.3). However, the total magnesium and iron column densities are estimated taking into account the jump across the respective edges, and they will not be affected by these problems. As expected, the RGS spectral fits provide a different $N_{\rm H}$ value than the simultaneous EPIC−RGS fit, because of the imperfect EPIC−RGS cross-calibration and the low resolution of EPIC, that smooth the absorption features (see Fig. 3).

3.2.2. The ionized gas

The fit residuals near 21.6 Å and 23.35 Å (see Fig. 4), where we should expect the 1s–2p transitions of O VII and O II respectively, suggest the presence of additional weak absorption features. Other weak features are found near 13.4 Å and 14.6 Å, close to the theoretical Ne IX and Ne II wavelengths. We deal separately with the different ionization states.

At first we made a fit to the RGS spectra adding columns of O II and Ne II to our model through a *slab* component. The *slab* model calculates the transmission of a layer of plasma with arbitrary composition. Free parameters are the intrinsic velocity dispersion and the column densities of the individual ions (Kaastra et al. 1996). The fits improve significantly: by fitting the two RGS observations simultaneously we get ΔC-stat $\sim$ 130. The velocity dispersion is not well constrained ($\sigma_V = 50 \pm 15$ km s^{-1}). The average ion columns are $1.2 \pm 0.4 \times 10^{21}$ m^{-2} (O II) and $2.4 \pm 0.4 \times 10^{21}$ m^{-2} (Ne II), while the cold gas gives $3.05 \pm 0.15 \times 10^{22}$ m^{-2} (O I) and $6.7 \pm 0.3 \times 10^{21}$ m^{-2} (Ne I).

In second instance we add another *slab* component to take into account the contribution by the hot gas. The columns are $1.1 \pm 0.5 \times 10^{20}$ m^{-2} (both O VII and O VIII) and $3.5 \pm 2.5 \times 10^{19}$ m^{-2} (Ne IX). The addition of the hot gas provides ΔC-stat = 30, which is significantly less than the improvement we obtained by adding the weakly ionized gas. Moreover we can only put an upper limit to the velocity dispersion of the hot ionized gas (250 km s^{-1}).

However, in order to take care of every absorption feature created by all ions in the warm-hot phases and to deal with physical models, we substituted the two *slab* components with two *hot* components. We coupled the elemental abundances of the warm-hot components to those of the cold gas, assuming all ISM phases have the same abundances. This is a reasonable assumption, especially for the warm (low-ionization) ionized gas, as its temperature is not too different from the temperature of warm neutral gas. The additional free parameters are the hydrogen column density, the temperature and the velocity dispersion. In summary, the additional warm and hot phases give an average improvement of ΔC-stat $\sim$ 80 for only six free parameters added. We label such a three-gas model as Model B and display all results in Table 3. We plot the individual absorption edges of O, Fe, Ne and Mg in Figs. 5–8, respectively. We discuss these results in Sect. 3.3. The predicted deviations near the oxygen and iron edges, clearly seen in Figs. 5 and 6, still confirm that pure

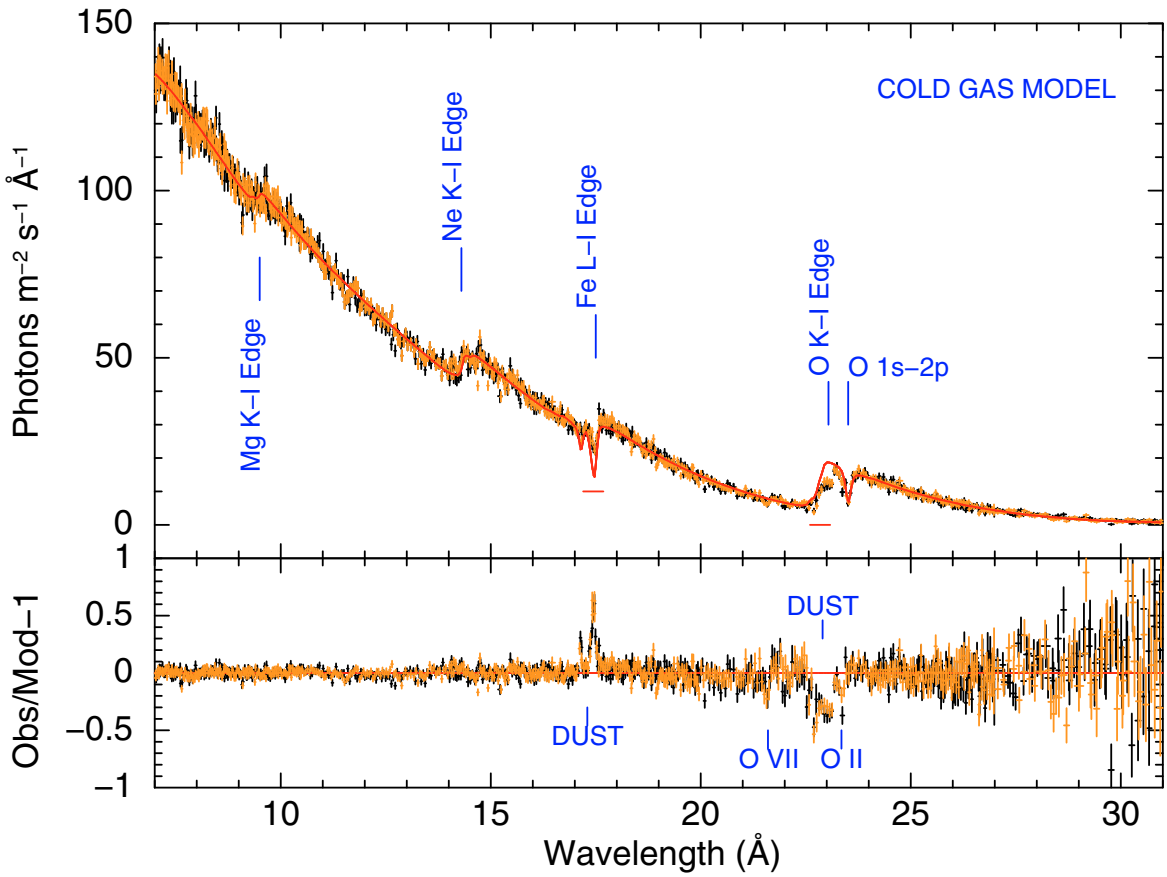

Fig. 4. Continuum best-fit to the RGS spectrum of the first (black) and the second (orange) observation. Here we use the simple model used for EPIC−RGS fits (see Sect. 3.1). In the fits we excluded two small regions near the O I K-edge and the Fe I L-edge (see Sect. 3.2), which are indicated by two red horizontal strips in the *top panel*. See Sect. 3.2.3 for the detailed analysis. The results of the fits are shown in Table 3, they refer to model A.

Table 3. RGS spectral fits to the persistent emission.

Component	Parameter	Mod A[a] OBS 1	Mod A[a] OBS 2	Mod A[a] OBS 1+2	Mod B OBS 1+2	Mod C OBS 1+2
Cold	N_H (10^{25} m^{-2})	4.18 ± 0.01	4.22 ± 0.07	4.21 ± 0.09	3.88 ± 0.07	3.94 ± 0.05
	kT (10^{-4} keV)	5.90 ± 0.14	6.13 ± 0.12	6.02 ± 0.09	6.04 ± 0.10	8.6 ± 0.4
	σ_V (km s^{-1})	27 ± 15	18 ± 6	13 ± 7	<12.6	<24
	O	1.30 ± 0.02	1.29 ± 0.02	1.29 ± 0.01	1.29 ± 0.02	1.17 ± 0.03
	Ne	2.08 ± 0.04	1.86 ± 0.07	1.95 ± 0.07	2.19 ± 0.10	1.75 ± 0.11
	Mg	2.27 ± 0.12	2.14 ± 0.16	2.21 ± 0.16	1.93 ± 0.15	1.30 ± 0.25
	Fe	1.39 ± 0.02	1.42 ± 0.06	1.39 ± 0.05	1.65 ± 0.08	<0.1
Warm	N_H (10^{25} m^{-2})	–	–	–	0.46 ± 0.06	0.15 ± 0.05
	kT (10^{-3} keV)	–	–	–	5.4 ± 0.3	4.5 ± 0.5
	σ_V (km s^{-1})	–	–	–	50 ± 25	<150
Hot	N_H (10^{25} m^{-2})	–	–	–	0.042 ± 0.008	0.047 ± 0.011
	kT (keV)	–	–	–	0.20 ± 0.02	0.20 ± 0.03
	σ_V (km s^{-1})	–	–	–	<160	<200
Dabs[b]	N_{Fe}	–	–	–	–	2.6 ± 0.1
	N_{Mg}	–	–	–	–	2.3 ± 0.1
Amol[b,c]	N_O (i = 14, Silicates)	–	–	–	–	2.5 ± 0.5
	N_O (i = 7, H_2O Ice)	–	–	–	–	<0.7
	N_O (i = 2, CO)	–	–	–	–	<0.4
	N_O (i = 23, Aluminates)	–	–	–	–	<0.4
Statistics	C-Stat / d.o.f.	2239/1595	2170/1589	4587/3232	4435/3226	4818/3398
	C-Stat / d.o.f. (*)	2930/1684	3040/1710	5757/3410	6064/3404	4818/3398

Notes. [(a)] We give the separate fits for the two observations only for Model A in order to show that they are consistent within the errors and thus can be fitted together. C-Stat/d.o.f. (*) Refers to the statistics obtained by including the wavelength ranges 17.2–17.7 Å and 22.7–23.2 Å, which in fits are ignored except in the case of the complete model. [(b)] All columns for the *dabs* and *amol* components are reported in units of 10^{21} m^{-2}. [(c)] Each *amol* component is displayed together with its molecular index as reported in Table A.1.

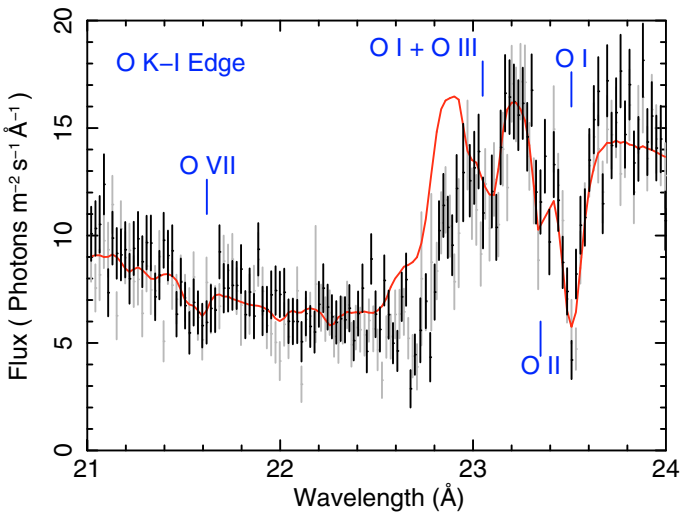

Fig. 5. O I K-edge: data and Model B. Black and grey points refer to the first and second observation, respectively.

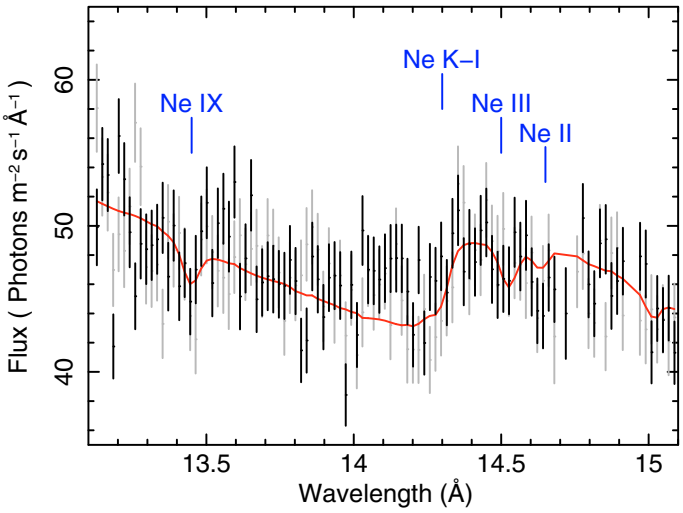

Fig. 7. Ne I K-edge: data and Model B.

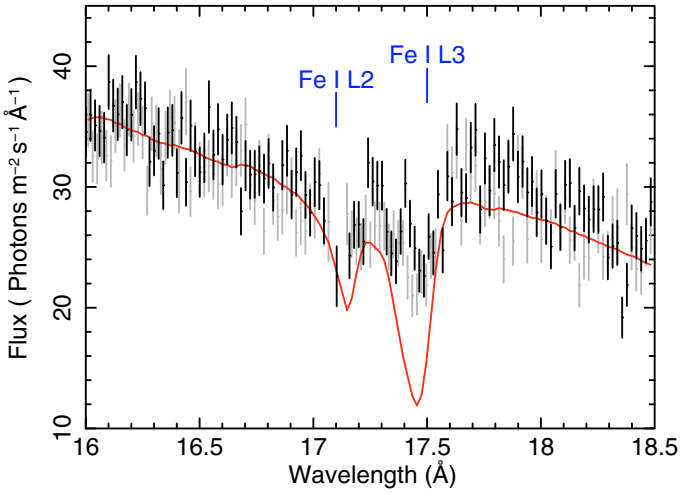

Fig. 6. Fe I L-edge: data and Model B.

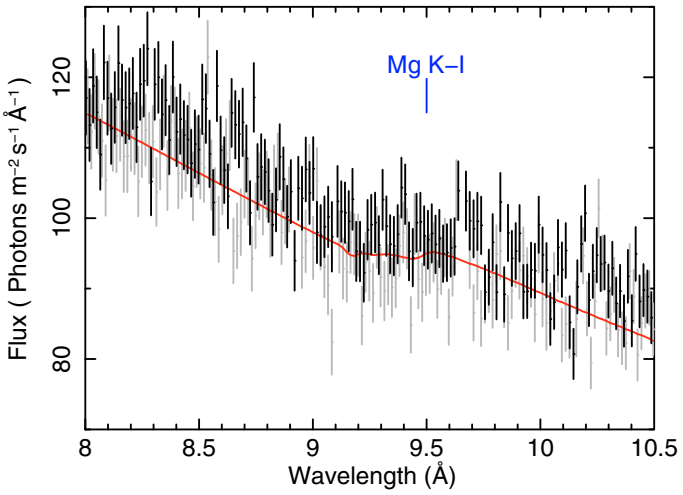

Fig. 8. Mg I K-edge: data and Model B.

interstellar gas cannot reproduce all the absorption features and that we need to take into account different states of matter, such as solids.

Finally, we also considered the model where the cold gas component is forced to be neutral by freezing its temperature to 5×10^{-4} keV, i.e. 5 800 K. In this case, we got an almost equal fit (C-stat/d.o.f. = 4466/3227), with the exception that the warm component has a significantly lower temperature ($\sim 1.4 \times 10^{-3}$ keV, i.e. 10–20 000 K), to account for the O II that in our nominal fit is partially produced by the cold component. This temperature value is more representative than our previous value of 5.4×10^{-3} keV for the warm ionized gas in the ISM (Ferrière 2001). However, both fits are acceptable, thus we report only results obtained with the cold-gas temperature as free parameter in Table 3.

3.2.3. Fine structures: dust and molecules

Further important improvements to our fit are obtained by adding both dust and molecules to our multiphase gas model. We use here two recently added models of SPEX: *dabs* and *amol*, which are briefly described below. The transmission of dust is calculated by the *dabs* model in SPEX: it accounts for the self-shielding of X-ray photons by dust grains, but uses the edge and line structure for atomic gas. It was first used in the analysis of the Crab spectrum by Kaastra et al. (2009). It follows completely the dust treatment as described by Wilms et al. (2000) and is useful to estimate the dust-to-gas column ratio and the depletion factor for several elements. We assume the default values for the grain parameters because they are physically acceptable: the grains are assumed to be spherical and fluffy, with density $\rho = 1000\,\mathrm{kg\,m^{-3}}$, grain radius a between $a_{\min} < a < a_{\max}$, where $a_{\min} = 0.025$ μm and $a_{\max} = 0.25$ μm, with a size distribution $\mathrm{d}n/\mathrm{d}a \sim a^{-p}$ and $p = 3.5$ (Kaastra et al. 2009). Including the *dabs* component in our model, we obtain a significant improvement to the fit by requiring at least ~90% of iron to be confined in dust grains (see Table 3). Inside the iron edge the shielding effect of dust is stronger than its fine structure features, and thus the *dabs* component is suitable to fit the data. Indeed, the ~4σ deviation at 17.4 Å (Fig. 6) and the ~1σ deviation near 17.1 Å, due to the assumption of a pure-gas ISM, just disappear (see Fig. 9). Moreover, from the *dabs* model we derive ~40% of the oxygen to be bound in dust grains. Unfortunately, this model does not yield a good fit of the oxygen edge, where strong features due to

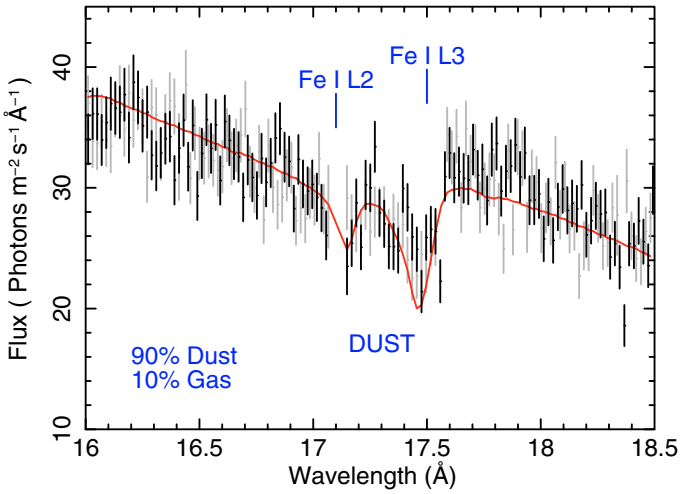

Fig. 9. Iron edge: data and Model C.

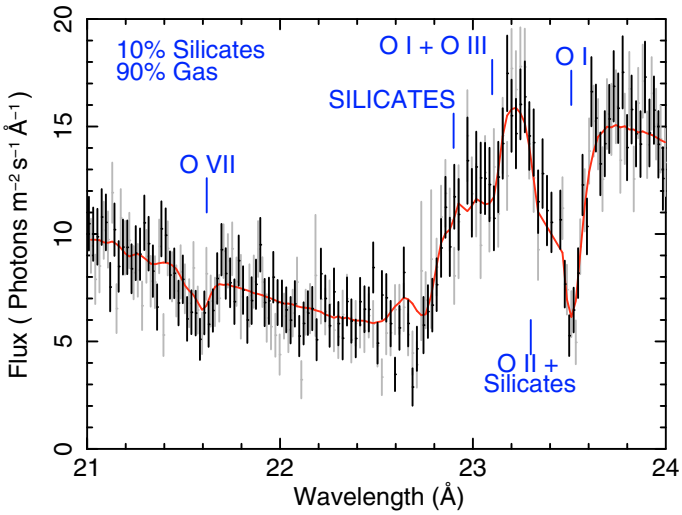

Fig. 10. Oxygen edge: data and Model C.

molecules are present that are not taken into account by the *dabs* model.

A much larger improvement is obtained when we introduce molecules and minerals containing oxygen atoms. For the first time we used the *amol* model in SPEX to take into account bound forms of oxygen. The model currently takes into account the modified edge and line structure around the O K-edge using measured cross sections of various compounds, taken from the literature. More details about this model can be found in Appendix A. The *amol* model is very useful to constrain the local molecular features, but it does not account for the dust shielding effects. We tried 23 different types of compounds such as CO, N_2O, H_2O, ice, FeO and several minerals. The best fit is obtained by using a mixture of silicates, such as andradite, and water ice plus other molecules (see Fig. 10 and Table 4). This additional component removes the previous 3 σ deviation of the pure-gas model between 22.7–23.0 Å inside the oxygen edge (Fig. 5). Finally we completed the dust model choosing the *amol* component for oxygen and *dabs* component for all the other depleted elements, such as iron and magnesium. The final gas+dust model describes the data much better than all previous models (see Figs. 9 and 10) and it allows us to estimate the dust-to-gas ratio. We label this model C and show the parameters in Table 3.

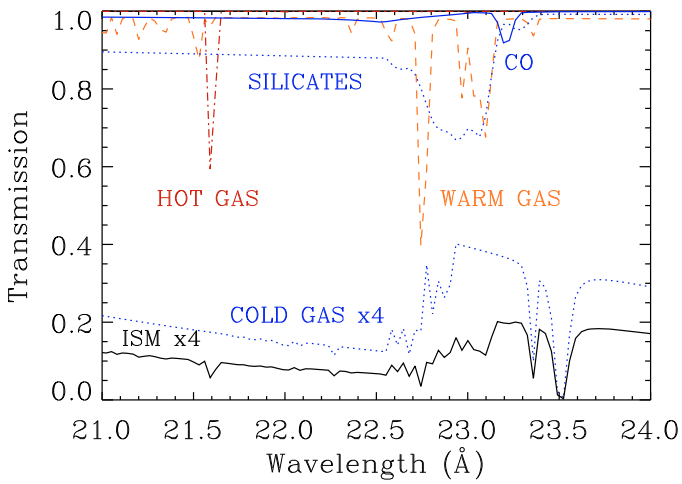

Fig. 11. Transmission near the O I K-edge. The model used is Mod C (see Sect. 3.2.3, Tables 3 and 6). Both cold-gas and entire-ISM transmission is multiplied by a factor of 4 for displaying purpose.

Table 4. Table of the contributions to the oxygen column-density.

Phase	Constituent	N_O (10^{22} m^{-2})	% of $N_O^{p\,a}$	% of $N_O{}^b$
Gas	O I	2.7 ± 0.1	94 ± 4	90 ± 6
	O II, O III, O IV	0.10 ± 0.05	4 ± 2	
	O VII, O VIII	0.05 ± 0.01	2.0 ± 0.5	
Dust	Silicates	0.25 ± 0.05	85–100	10 ± 2
	Aluminates	<0.04	0–15	
Molecules	H_2O ice	<0.07	~65	0–2
	CO	<0.04	~35	

Notes. $^{(a)}$ % of N_O^p represents the contribution of each constituent to the respective phase. $^{(b)}$ % of N_O give the contribution of the different phases to the total oxygen column density. See also Sect. 3.2.3 and Fig. 11 for the transmission of the main compounds.

3.3. ISM model complexity

The spectral modeling indicates that in the line of sight towards our X-ray source the ISM is much more complex than simple neutral gas. The gas is rather structured in different phases and dust also consists of various compounds.

The gas consists of three components (see Table 3): cold gas with a temperature $kT \sim 5–10 \times 10^{-4}$ keV ($5.8–10 \times 10^3$ K), warm ionized gas with $kT \sim 1–5 \times 10^{-3}$ keV ($1–6 \times 10^4$ K) and hot ionized gas with $kT \sim 0.2$ keV ($\gtrsim 2 \times 10^6$ K). The column densities N_H of these three components span over 2 orders of magnitude: the cold gas accounts for ~90–95% of the total column N_H^{tot}, N_H^{warm}~5–10% of N_H^{tot}, while the hot gas contributes ~1%.

The warm component produces the low-ionization absorption lines of O II and O III, at 23.35 Å and 23.1 Å respectively (see Fig. 5). It also provides a better modeling of the neon edge (see Fig. 7). Using model B we estimate $N_{O\,II} = 2.0 \pm 0.5 \times 10^{21}$ m^{-2} and $N_{O\,III} = 1.4 \pm 0.5 \times 10^{21}$ m^{-2}, respectively ~7% and ~5% of the total oxygen column. However, the derived column density of the warm ionized gas is affected by the presence of dust and molecules in the line of sight. Indeed, the absorption features that we see near 23.35 Å and 23.1 Å are contaminated by dust and molecule effects. Contributions from dust and molecules (Model C in Table 3) are confirmed by the improvements to the fit (see also Figs. 9 and 10), and the column density of the warm gas is finally reduced to about 5% of the full gas column (see Table 4).

Table 5. Average ISM abundances in units of the protosolar values (Lodders 2003) and calculated by summing contribution from all ISM phases.

X	O	Ne	Mg	Fe	N[e]
GS 1826-238[a]	1.23 ± 0.05	1.75 ± 0.11	2.45 ± 0.35	1.37 ± 0.17	2.4 ± 0.7
Crab[b]	1.030 ± 0.016	1.72 ± 0.11	0.85 ± 0.21	0.78 ± 0.05	1.01 ± 0.09
Cyg X-2[c]	0.6–0.8	0.8–1.1	0.6–1.1	–	–
4U 1820-303[d]	0.7–1.1	1.1–2.0	–	0.3–0.8	–

Notes. [(a)] Model C, gas + dust. [(b)] Kaastra et al. (2009) Model B, gas + dust. [(c)] Yao et al. (2009). [(d)] Juett et al. (2006). [(e)] Estimated through a local fit in the 27–33 Å range.

Table 6. Ionic column densities of oxygen in 10^{22} m^{-2}.

X	Mod A_{sim}[a]	Mod A[a]	Mod B[b]	Mod C[c]
O I	3.0	3.1	2.9	2.7
O II, O III, O IV	≡0	≡0	0.35	0.1
O VII, O VIII	≡0	≡0	0.05	0.05
Dust	≡0	≡0	≡0	0.35
Total N_O	3.0	3.1	3.3	3.2

Notes. [(a)] Mono-phase gas (Table 3 for the simultaneous EPIC-RGS fit). [(b)] Three-phases gas (Table 3). [(c)] Gas + dust model (see Table 4). The agreement between the oxygen column densities estimated with different models validates our method.

The column density of hot gas is about two orders of magnitude lower than the cold gas column and its temperature is around two million K. As expected, the hotter gas has a higher velocity dispersion (see Table 3). The hot gas model gives a good fit of the O VII absorption line at 21.6 Å, together with the small feature at 13.4 Å produced by Ne IX.

According to the analysis of the oxygen edge, the solid phase of the ISM towards GS 1826–238 consists of a mixture of minerals (such as andradite silicates) and traces of CO and water ice. We cannot yet distinguish between amorphous and crystalline phases. As reported in Table 4 the bulk of the oxygen, ~90%, appears to be in the gas phase, while the remaining ~10% is made mostly of solids, such as silicates and water ice. Obviously, there could be substances able to reproduce these features in the spectrum other than our few dozen test molecules. For the iron, instead, we obtain a different composition: at least ~90% of Fe appears to be bound in dust grains. In our dust model we assume a depletion factor of 0.8 for magnesium, as suggested by Wilms et al. (2000). The derived gas ($2.0 \pm 0.4 \times 10^{21}$ m^{-2}) and dust ($2.3 \pm 0.1 \times 10^{21}$ m^{-2}) column densities for the Mg are identical within the errors (see also Table 3).

3.4. ISM abundances

We estimated the abundances of Mg, Ne, Fe, O, and N (Table 5). The column density of each element refers to the sum of the contributions from all gas and dust phases. The abundances do not differ significantly between the two observations (see Table 3). This is expected if the absorption is mainly caused by the interstellar medium, because the ISM is stable on short timescales. The zero shift of the O I line, the position of the O, Fe, Ne, and Mg edges (see Figs. 5 to 10) and the low velocity dispersion suggest that the absorber matter is a mixture of gas and dust without outflows or inflows, not broadened owing to Keplerian motion around the X-ray source. This is also consistent with an ISM origin. For a more detailed discussion on the abundances and comparisons with previous work see Sect. 4.3.

A separate analysis is required for the nitrogen edge at 30.8 Å. Indeed, at wavelengths higher than 29 Å the source flux decreases significantly and is comparable to the background. Thus, the spectrum around the N I K-edge is noisy and the N I column density has a large uncertainty. We decided to freeze the continuum parameters and try either a broadband fit to the range 7–33 Å or a local fit between 27–33 Å. The abundance estimates are consistent within the error. Their average is reported in Table 5.

4. Discussion

4.1. The continuum

Our analysis shows that the persistent state of the low-mass X-ray binary GS 1826−238 is well represented by a double comptonization (C1+C2) plus a blackbody (BB) emission component, all three absorbed by the interstellar medium composed of a three-phases gas, dust and molecules (see Tables 2 and 3). In both observations the fits agree: all the ISM parameters appear to be fully consistent, thus we can discuss the results from the simultaneous fit of the high-resolution RGS data.

4.2. ISM structure

In Sect. 3.3 we showed that in our line of sight the ISM has a clear multiphase structure. There are media with different ionization states, dust grains, and molecules. As confirmed by Fig. 11, the bulk of the matter responsible for X-ray absorption is found in the form of *cold* gas with a temperature ~7000 K and low-velocity dispersion ($\sigma_V \lesssim 13$ km s^{-1}). At this temperature the gas is almost neutral: only iron and magnesium are partially ionized. Part of the cold matter is found in solid compounds, such as *dust grains* and *molecules*. Most of the iron is bound in dust grains. About 10% of the oxygen is found in compounds: the silicates contribute up to ~80% of this phase, while the remaining fraction consists of a mixture of other oxides (such as iron aluminates) together with ices and CO molecules in similar quantities (see Table 4). The best fit is obtained using as compound the andradite silicate $Ca_3 Fe_2 (SiO_4)_3$, but we need higher signal-to-noise data to distinguish among the different silicates, because also olivine and pyroxene are good candidates. Moreover, at the present stage our model does not take into account simultaneously the shielding and fine structure effects of oxygen compounds, thus the fraction of oxygen bound in solids could be higher, e.g. up to 40% (see Sect. 3.2.3). However, we are working to the development of models that take into account all the possible effects and we postpone a deeper analysis of the oxygen dust phase to a forthcoming paper.

About 5% of the gas is ionized (see Mod C in Table 3). Most of it is a *warm* plasma with $T \sim 10$–$50\,000$ K. It has a low-ionization degree and accounts for the interstellar O II and O III. Only 1–2% of the ISM gas appears to be highly ionized. Such a *hot* plasma reaches temperatures of $\sim 2 \times 10^6$ K and contributes to all O VII and O VIII present in the ISM. As we expect, the higher the temperature of the gas phase, the higher its velocity

dispersion. Unfortunately the velocity dispersion is not well constrained, especially for the hot ionized gas. This is not surprising because the lines are unresolved.

4.3. Comparison with previous results

4.3.1. ISM constituents

The average total column density of the multi-phase gas we estimate is about $(4.14 \pm 0.07) \times 10^{25}$ m^{-2}. This is not consistent with the value of $(3.19 \pm 0.01) \times 10^{25}$ m^{-2} found by Thompson et al. (2008). They combined data from Chandra, *XMM-Newton* and RXTE in the 0.5–100 keV band, but we know that the bulk of the absorption is at lower energy. Instead we have used both EPIC and RGS data. The latter detector has a higher spectral resolution between 0.3–2 keV and allows us to better estimate the absorption column. Also, Thompson et al. (2008) used the Morrison & McCammon (1983) model to fit the absorbing medium, which takes into account only contribution by cold neutral gas. In Sect. 3.1 we have shown that this model is not optimal, because it does not include lines. Furthermore, abundances and temperature cannot be free parameters. Instead our estimate of $N_{\rm H}$ is obtained by summing the contribution from all phases of the gas and by accounting for all absorption features found in the spectrum.

The multiphase structure of the ISM that we constrained is consistent with recent results (Ferrière 2001; Yao & Wang 2006; Yao et al. 2009). First of all, there is a good agreement in the fractions between the cold, warm, and hot phases of the gas. In particular the estimated amount of O VII, $\sim 1.6 \times 10^{20}$ m^{-2}, is fully consistent with the value found by Yao & Wang (2006) by fitting both O VII 1s−2p and 1s−3p lines in the spectrum of 4U 1820−303, which is another LMXB near the center of the Galaxy. The hot gas accounts for 1–2% of the total column density and represents the average fraction of hot plasma in the Galaxy. Indeed it agrees with previous estimates and can be fully explained by the heating of supernovae (McCammon & Sanders 1990). The velocity dispersion σ_V estimates agree with recent work. Yao & Wang (2006) combined oxygen and neon ionization lines in the *Chandra* spectrum of the LMXB 4U 1820−303, obtaining $\sigma_V < 350$ km s^{-1}. Juett et al. (2004) found $\sigma_V < 200$ km s^{-1} from oxygen lines fits to the *Chandra* spectra of several LMXBs.

Moreover, we found clear indications of dust depletion in some heavy elements, such as oxygen, iron, and magnesium. According to the different dust models that we used (*dabs* and *dabs+amol*), we find ∼50% of Mg, more than 90% of Fe and 10–40% of oxygen in the form of dust grains and molecular compounds. These results are mostly consistent with previous estimates (Wilms et al. 2000; Kaastra et al. 2009). The iron dust-to-gas ratio found towards GS 1826−238 is among the highest measured in the Galaxy. Williams & Taylor (1996) showed that the higher the density of a molecular cloud, the higher is the probability of forming dust and molecules from gas particles. Thus the higher dust-to-gas ratio we estimated towards the center of the Galaxy suggests high-density regions.

The presence of silicates and ice in the ISM, constrained by the O I K-edge analysis, is supported by other work. Paerels et al. (2001) found similar features within 22.7–23.0 Å in the spectrum of the LMXB X0614+091, and they argued that it should be due to iron oxides or oxygen generally bound in dust. Costantini et al. (2005) found indications of silicates such as olivine and pyroxene by modeling the feature of the scattering halo of Cyg X−2. Recently, de Vries & Costantini (2009) found evidence for EXAFS in the short-wavelength side of the oxygen edge in the spectrum of Sco X−1, and their results suggest the presence of amorphous water ice.

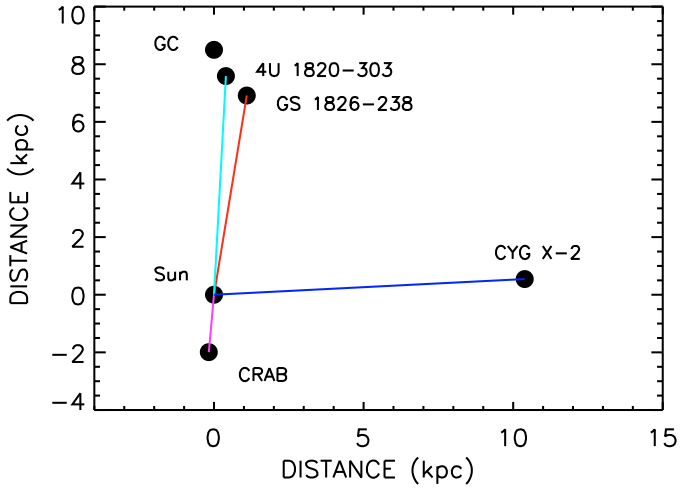

Fig. 12. Map of the X-ray sources compared in this paper. GC is the Galactic Center and the Sun is assumed to be 8.5 kpc far away from it.

We have checked CO surveys (Dame et al. 2001) in order to test the presence of molecular clouds. There is no clear evidence for these clouds in our line of sight $(x, y)_{\rm GAL} \sim (9.3°, -6.1°)$, while there is an important amount of diffuse dust (see also Schlegel et al. 1998). This is consistent with the fact that we can only put upper limits to ice and CO columns. Thus the absorption should arise from a solid phase consisting mostly of minerals.

4.3.2. ISM abundances

The abundances are displayed in Table 5, they are reported relative to the recommended protosolar values of Lodders (2003). We also show the abundances obtained by Juett et al. (2006) towards the LMXB 4U 1820−303, which like GS 1826−238 is close to the Galactic center. Even more interesting is the comparison with the abundances estimated by Kaastra et al. (2009) in the direction of the Crab nebula and those estimated by Yao et al. (2009) towards Cyg X−2, which are two different lines of sight in our Galaxy (see the map in Fig. 12).

The derived abundances slightly depend on the model used: the *pure-gas* model and the complete *gas+dust* model yield different results on Ne, Fe, and Mg (Table 3). First, their abundances are more uncertain than the oxygen abundance. Secondly, Fe and Mg are the most depleted elements: as dust grains give rise to absorption features different from gas particles, modeling the edges of highly depleted elements provides different results if we account for dust effects or not. These deviations are probably intensified because we observed through a high-density region: here high metal depletion is expected (Williams & Taylor 1996).

All the heavy elements are over-abundant with respect to the protosolar values. Neon is over-abundant by a factor ∼1.7, as found by Kaastra et al. (2009) in the *XMM-Newton* observations of the Crab nebula. The solar abundance of neon is probably under-estimated (see Lodders & Palme 2009), so our estimate may be not really different from the real solar value. As we will show in the next paragraph, the metallicity gradient could also be responsible for part of the Ne over-abundance.

The reason for the over-abundances of O, Fe, and Mg is rather different from the neon excess. First of all, we are able to

measure both gas and dust contributions for O, Fe and Mg, without the risk of missing important fractions. Secondly, deviations in the abundances with respect to the average Galactic values are also due to their metallicity gradient. If $A(X)$ is the abundance of a certain element X in the vicinity of GS 1826−238, we can write (see Esteban et al. 2005)

$$\frac{A(X)}{A(X)_\odot} = 10^{\alpha_X\,(D_{\rm GS} - D_\odot)}, \quad (1)$$

where $D_\odot$ and $D_{\rm GS}$ are the galactocentric radii of the Sun and GS 1826−238, respectively ∼8.5 kpc and ∼2 kpc; α_X is the abundance gradient of the element along the line of sight and $A(X)_\odot$ is its abundance near the Sun. In this way, we can compare our estimates of abundance changes with the values predicted by the gradient estimates. Unfortunately, the gradient estimates in the literature are quite uncertain and are available only for a limited range of radii, i.e. between 4–16 kpc (see Pedicelli et al. 2009). Thus we can trust only in the abundance changes in 4–5 kpc along our line of sight. Moreover, the column density estimated for each element refers to its integral along the line of sight, where we also expect a density increase towards the Galactic Center. Because the density increases towards the Galactic center, the predicted abundance at the galactocentric distance of GS 1826−238 should be close to the weighted average abundance along the sightline:

- Oxygen is over-abundant by about 20–30% (see Table 5). According to Esteban et al. (2005), the oxygen gradient is $\alpha_{\rm O} = (-0.04 \pm 0.01)\,{\rm kpc}^{-1}$, which should provide an increment (Eq. (1)) of at least ∼32% in the oxygen abundance. This is consistent with our estimate.
- The iron abundance ∼1.20–1.54 (see Table 5) almost agrees with the ≳50% increment derived by the accepted iron gradient in the Galactic disk $\alpha_{\rm Fe} = (-0.06 \pm 0.02)$ kpc^{-1} (Friel et al. 2002; Pedicelli et al. 2009).
- Neon is over-abundant by more than 70%. It is difficult to compare it with the Galactic gradient because this is quite uncertain, on average $\alpha_{\rm Ne} = (-0.06 \pm 0.04)$ kpc^{-1} (Simpson et al. 1995; Maciel & Quireza 1999). From Eq. (1) we predict a lower limit $A({\rm Ne}) \sim 1.3$. The sum of this a value to the revisited protosolar abundance ($\Delta A({\rm Ne}) \sim 30\%$, see Lodders & Palme 2009) provides $A({\rm Ne}) \sim 1.6$, which is fully consistent with our estimate. This result suggests that the neon over-abundance that we constrain is due to both the Galactic gradient and the previous under-estimate found in the literature.
- Nitrogen shows a steeper Galactic gradient of about ∼− 0.08 kpc^{-1} (Gummersbach et al. 1998), which provides $\Delta A({\rm N}) \sim 100\%$ (Eq. (1)) and agrees with our estimate (see Table 5). Of course, both of them are quite uncertain and we are not able to provide more information.
- Also magnesium should be at least twice the protosolar value as we found (see Table 5). However, it is difficult to compare our result with the Mg Galactic gradient found in the literature, because the results differ widely in the literature (Rolleston et al. 2000). According to Gummersbach et al. (1998) $\alpha_{\rm Mg} \sim -0.08$ kpc^{-1}, which together with Eq. (1) implies an abundance increment of at least 100%. This is fully consistent with what we found.

The iron and oxygen abundances towards 4U 1820−303 (Table 5) appear to disagree with our results despite its similar location near the Galactic center. Juett et al. (2006) attribute this low iron abundance to depletion into dust grains in the interstellar medium, and they also report that oxygen could be middle-depleted. In Sect. 3.2.3 we have shown that iron is among the most depleted elements in the ISM, oxygen is also partially depleted and a pure-gas model cannot reproduce all the ISM spectral features. This indicates that the differences between the Fe and O abundances are due to the capability of our gas+dust model to measure the contribution from solid phases, which are absent in the pure-gas model of Juett et al. (2004, 2006).

The Crab nebula is relatively close to the Solar System, i.e. ∼2 kpc, but opposite to the Galactic Center (see Fig. 12). Thus we expect abundances close to the protosolar values of Lodders (2003), which is just what Kaastra et al. (2009) found.

The source LMXB Cyg X-2 is also far away from the center of the Galaxy and about 10 kpc away from the Sun. The abundances estimated for this source are lower than those measured towards the Crab and GS 1826−238 (see Table 5). This agrees with the assumed abundance gradients we have discussed.

In summary, the differences with respect the protosolar abundances that we estimate are consistent with the literature. The increase of metallicity towards the center of the Galaxy should be due to evolutionary effects like supernovae explosions, which enrich the ISM with heavy elements, especially in the higher density region of the bulge and the disk of our Galaxy. A deeper analysis is required: we need to study more sources, even in the same region, and further improve our models in order to account for every contribution to the column densities.

5. Conclusion

We have presented a complete treatment of the interstellar medium towards the low-mass X-ray binary GS 1826−238, which is a bright X-ray source near the Galactic Center. We have shown that in the line of sight the ISM is composed of a complex mixture of a multi-phase gas, dust, and molecules.

The gas is almost neutral and the ionization degree is about 5%. Significant fractions of the column density of some heavy elements are in the form of molecules or dust grains: at least 10% of oxygen, 50% of magnesium, and 90% of iron. Such a solid phase should consist of a mixture of silicates (≳60%), CO (≲10%), ice (≲20%) and other iron oxides (≲10%).

We have found over-abundances for all the elements for which we have been able to measure the individual column density. The Ne over-abundance that we estimate is consistent with other recent work in different lines of sight, such as towards the Crab (Kaastra et al. 2009), suggesting that the solar value is underestimated. However, our agreement with the predicted Ne gradient in the Galaxy is also consistent with an abundance increase owing to stellar evolution: towards the Galactic center there are high-density regions with evolved star that could have enriched the ISM with heavy elements such as neon.

Differently from the previous X-ray spectroscopy work, we have found over-abundances for oxygen (1.2), iron (1.4) and magnesium (2.4). These elements are also in the form of dust and molecules. Thus our estimates are partially due to the fact that we are also able to measure the contributions from the solid phase. The abundance of metals agrees with the metallicity gradients and shows the chemical inhomogeneity of the interstellar medium.

The diagnostic of the ISM constituents fits the predicted models for both its thermal and chemical structures, showing a good agreement with the current state of art (Ferrière 2001). The dust column is consistent with the multi-wavelength, X-ray versus IR, observations. All this supports our research method and justifies new observations and analyses of other sources in

Table A.1. Molecules present in the *amol* model.

Nr	Name	Chemical formula	Reference
1	molecular oxygen	O_2	a
2	carbon monoxide	CO	a
3	carbon dioxide	CO_2	a
4	laughing gas	N_2O	a, b
5	water	H_2O	c
6	crystalline ice	H_2O	d
7	amorphous ice	H_2O	d
8	cupric oxide	CuO	e
9	nickel monoxide	NiO	e
10	iron oxide	$Fe_{1-x}O$	e
11	magnetite	Fe_3O_4	e
12	hematite	Fe_2O_3	e
13	eskolaite	Cr_2O_3	e
14	andradite	$Ca_3Fe_2Si_3O_{12}$	e
15	acmite	$NaFeSi_2O_6$	e
16	franklinite	$Zn_{0.6}Mn_{0.8}Fe_{1.6}O_4$	e
17	chromite	$FeCr_2O_4$	e
18	ilmenite	$FeTiO_3$	e
19	perovskite	$CaTiO_3$	e
20	olivine	$Mg_{1.6}Fe_{0.4}SiO_4$	e
21	almandine	$Fe_3Al_2(SiO_4)_3$	e
22	hedenbergite	$CaFeSi_2O_6$	e
23	hercynite	$FeAl_2O_4$	e

References. [a] Barrus et al. (1979), 0.5–0.75 eV resolution. [b] Wight & Brion (1974), 0.5 eV resolution. [c] Hiraya et al. (2001), 0.055 eV resolution. [d] Parent et al. (2002), 0.1 eV resolution. [e] van Aken et al. (1998), 0.8 eV resolution

different lines of sight. These analyses provide indeed a better mapping of the ISM and a deeper study of its chemical composition, together with its role in the evolution of the entire Galaxy.

Acknowledgements. We are grateful to Jean in't Zand for the useful discussion and clarification about the physics of low-mass X-ray binaries. This work is based on observations obtained with *XMM-Newton*, an ESA science mission with instruments and contributions directly funded by ESA Member States and the USA (NASA). SRON is supported financially by NWO, the Netherlands Organization for Scientific Research.

Appendix A: Absorption by oxygen molecules

The *amol* model calculates the transmission of various molecules. Presently only the oxygen edge is taken account of. Updates of this model, once made, will be reported in the manual of SPEX. The following compounds are presently taken into account (see Table A.1).

The chemical composition of these minerals was mainly taken from the Mineralogy Database of David Barthelmy[4]. We take the cross-sections from the references as listed in Table A.1 in the energy interval where these are given, and use the cross section for free atoms Verner & Yakovlev (1995) outside this range. van Aken et al. (1998) do not list the precise composition of iron oxide. We assume here that $x = 0.5$.

Some remarks about the data from Barrus et al. (1979): not all lines are given in their tables because they suffered from instrumental effects (finite thickness absorber combined with finite spectral resolution). However, Barrus et al. have estimated the peak intensities of the lines based on measurements with different column densities, and they also list the *FWHM* of these transitions. We have included these lines in the table of cross sections and joined smoothly with the tabulated values.

[4] http://webmineral.com/

For N_2O, the fine structure lines are not well resolved by Barrus et al. Instead we take here the relative peaks from Wight & Brion (1974), that have a relative ratio of 1.00:0.23:0.38:0.15 for peaks 1, 2, 3, and 4, respectively. We adopted equal *FWHM*s of 1.2 eV for these lines, as measured typically for line 1 from the plot of Wight & Brion (1974). We scale the intensities to the peak listed by Barrus et al. (1979). Further, we subtract the C and N parts of the cross section as well as the oxygen 2s/2p part, using the cross sections of Verner & Yakovlev (1995). At low energy, a very small residual remains, which we corrected for by subtracting a constant fitted to the 510–520 eV range of the residuals. The remaining cross section at 600 eV is about 10% above the Verner cross section; it rapidly decreases; we approximate the high-E behavior by extrapolating linearly the average slope of the ratio between 580 and 600 eV to the point where it becomes 1.

References

Barrus, D. M., Blake, R. L., Burek, A. J., Chambers, K. C., & Pregenzer, A. L. 1979, Phys. Rev. A, 20, 1045
Costantini, E., Freyberg, M. J., & Predehl, P. 2005, A&A, 444, 187
Dame, T. M., Hartmann, D., & Thaddeus, P. 2001, ApJ, 547, 792
de Vries, C. P., & Costantini, E. 2009, A&A, 497, 393
de Vries, C. P., den Herder, J. W., Kaastra, J. S., et al. 2003, A&A, 404, 959
den Herder, J. W., Brinkman, A. C., Kahn, S. M., et al. 2001, A&A, 365, L7
Esteban, C., García-Rojas, J., Peimbert, M., et al. 2005, ApJ, 618, L95
Ferrière, K. M. 2001, Rev. Mod. Phys., 73, 1031
Friel, E. D., Janes, K. A., Tavarez, M., et al. 2002, AJ, 124, 2693
Gummersbach, C. A., Kaufer, A., Schaefer, D. R., Szeifert, T., & Wolf, B. 1998, A&A, 338, 881
Heger, A., Cumming, A., Galloway, D. K., & Woosley, S. E. 2007, ApJ, 671, L141
Hiraya, A., Nobusada, K., Simon, M., et al. 2001, Phys. Rev. A, 63, 042705
in't Zand, J. J. M., Keek, L., Cumming, A., et al. 2009, A&A, 497, 469
Juett, A. M., Schulz, N. S., & Chakrabarty, D. 2004, ApJ, 612, 308
Juett, A. M., Schulz, N. S., Chakrabarty, D., & Gorczyca, T. W. 2006, ApJ, 648, 1066
Kaastra, J. S., Mewe, R., & Nieuwenhuijzen, H. 1996, in UV and X-ray Spectroscopy of Astrophysical and Laboratory Plasmas, ed. K. Yamashita & T. Watanabe, 411
Kaastra, J. S., de Vries, C. P., Costantini, E., & den Herder, J. W. A. 2009, A&A, 497, 291
Lodders, K. 2003, ApJ, 591, 1220
Lodders, K., & Palme, H. 2009, Meteoritics and Planetary Science Supplement, 72, 5154
Maciel, W. J., & Quireza, C. 1999, A&A, 345, 629
McCammon, D., & Sanders, W. T. 1990, ARA&A, 28, 657
Morrison, R., & McCammon, D. 1983, ApJ, 270, 119
Paerels, F., Brinkman, A. C., van der Meer, R. L. J., et al. 2001, ApJ, 546, 338
Parent, P., Laffon, C., Mangeney, C., Bournel, F., & Tronc, M. 2002, J. Chem. Phys., 117, 10842
Pedicelli, S., Bono, G., Lemasle, B., et al. 2009, A&A, 504, 81
Rolleston, W. R. J., Smartt, S. J., Dufton, P. L., & Ryans, R. S. I. 2000, A&A, 363, 537
Schattenburg, M. L., & Canizares, C. R. 1986, ApJ, 301, 759
Schlegel, D. J., Finkbeiner, D. P., & Davis, M. 1998, ApJ, 500, 525
Simpson, J. P., Colgan, S. W. J., Rubin, R. H., Erickson, E. F., & Haas, M. R. 1995, ApJ, 444, 721
Strüder, L., Briel, U., Dennerl, K., et al. 2001, A&A, 365, L18
Thompson, T. W. J., Galloway, D. K., Rothschild, R. E., & Homer, L. 2008, ApJ, 681, 506
Ubertini, P., Bazzano, A., Cocchi, M., et al. 1999, ApJ, 514, L27
van Aken, P. A., Liebscher, B., & Styrsa, V. J. 1998, Physics and Chemistry of Minerals, 25, 494
Verner, D. A., & Yakovlev, D. G. 1995, A&AS, 109, 125
Wight, G., & Brion, C. 1974, Journal of Electron Spectroscopy and Related Phenomena, 3, 191
Williams, D. A., & Taylor, S. D. 1996, QJRAS, 37, 565
Wilms, J., Allen, A., & McCray, R. 2000, ApJ, 542, 914
Yao, Y. & Wang, Q. D. 2006, ApJ, 641, 930
Yao, Y., Schulz, N. S., Gu, M. F., Nowak, M. A., & Canizares, C. R. 2009, ApJ, 696, 1418